Observations and modeling of ice cloud shortwave spectral albedo during the Tropical Composition, Cloud and Climate Coupling Experiment

Bruce C. Kindel*[,1,2], K. Sebastian Schmidt[2], and Peter Pilewskie[1,2]
Department of Atmospheric and Oceanic Sciences[1]
Laboratory for Atmospheric and Space Physics[2]
University of Colorado-Boulder
Boulder, CO

Bryan A. Baum
Space Science and Engineering Center
University of Wisconsin-Madison
Madison, WI

Ping Yang
Department of Atmospheric Sciences
Texas A&M University
College Station, TX

Steve Platnick
NASA Goddard Space Flight Center
Greenbelt, MD

* Corresponding author address:

Bruce Kindel
University of Colorado-Boulder
Boulder, CO
Email: kindel@lasp.colorado.edu

Abstract

Ice cloud optical thickness and effective radius is retrieved from hyperspectral irradiance and discrete spectral radiance measurements for four ice cloud cases during TC[4] over a range of solar zenith angle (23 ^{o} to 53^{o}) and high (46-90) and low (5-15) optical thicknesses. The retrieved optical thickness and effective radius using measurements at only two wavelengths from the Solar Spectral Flux Radiometer (SSFR) Irradiance and the MODIS Airborne Simulator (MAS) was input to a radiative transfer model using two libraries of ice crystal single scattering optical properties to reproduce spectral albedo over the spectral range from 400 to 2130 nm. The two commonly used ice single scattering models were evaluated by examining the residuals between observed spectral and predicted spectral albedo. The SSFR and MAS retrieved optical thickness and effective radius were in close agreement for the low to moderately optically thick clouds with a mean difference of 3.42 in optical thickness (SSFR lower relative to MAS) and 3.79 μm in effective radius (MAS smaller relative to SSFR). The higher optical thickness case exhibited a larger difference in optical thickness (40.5) but nearly identical results for effective radius. The single scattering libraries were capable of reproducing the spectral albedo in most cases examined to better than 0.05 for all wavelengths. Systematic differences between the model and measurements increased with increasing optical thickness and approached 0.10 between 400-600 nm and selected wavelengths between 1200-1300 nm. Differences between radiance- and irradiance-based retrievals of optical thickness and effective radius error sources in the modeling of ice single scattering properties are examined.

1. Introduction

Ice clouds play an important role in the radiative budget of the Earth's atmosphere [*Chen et al*., 2000, *Ramanathan et al.*, 1989] for example. The scattering and absorption of solar radiation reduces the amount of energy reaching the surface and thus has a cooling effect. Conversely, in the terrestrial thermal infrared wavelengths, ice clouds absorb radiation and emit at a lower temperature than the Earth's lower atmosphere and surface. This reduces the amount of energy radiated to space, increases the downward infrared radiation, and warms the surface. Whether ice cloud net effect is cooling or heating is dependent on several factors including cloud height, cloud thickness, and cloud microphysics [*Stephens et al.,* 1990, *Ebert and Curry*, 1992; *Jensen et al.,* 1994], for example. Ice cloud microphysical and optical properties that determine the radiative properties of clouds are perhaps the least well understood of these.

Liquid water cloud radiative transfer calculations utilize Lorenz-Mie theory, an exact computational method for calculating the single scattering properties (e.g. single scattering albedo and phase function or its first moment asymmetry parameter) of homogeneous spheres. In contrast to liquid water droplets, non-spherical ice cloud particles encompass a wide variety of shapes and sizes and thus computing their radiative properties must rely on more involved numerical techniques. To this end, extensive modeling and some measurements of ice crystal single scattering properties have been undertaken *[Takano and Liou,* 1989*; Macke et al.,* 1996*; Baum et al.*, 2005; *Yang and Liou* 1998; *Yang et al.* 2003; *Yang et al.*, 1997; *Mishchenko et al.,* 1996] and continues to be an area of active research. These models are used for satellite remote sensing retrievals of cloud optical properties (e.g. MODIS, AVHRR, etc) [*King et al.*, 1992; *Platnick et al*., 2003]. Ultimately, these types of satellite retrievals are used: as inputs to climate models to properly parameterize ice cloud radiative effects [*Stephens, et al.,* 1990], to potentially improve ice water parameterization in global circulation models [*Waliser, et al.*, 2009], and to aid in the study of ice cloud processes [*Jiang, et al.*, 2009].

Satellite remote sensing retrievals are, by necessity, radiance based and implement observations from discrete wavelength bands distributed across the solar and terrestrial spectrum. A selection of channels from radiance-based remote sensing instruments is, by itself, insufficient to completely determine the effects of clouds on the Earth's radiation budget. In practice, irradiance cannot be measured directly from space-borne platforms in low Earth orbit. It is, however, measured from aircraft. To bridge the fundamental geometrical and spectral differences between satellite measurements of discrete-band radiance and the more energetically relevant quantity, continuous spectral irradiance, field campaigns deploying instruments that measure discrete-band radiance and hyperspectral irradiance have been conducted: the Ice Regional Study of Tropical Anvils and Cirrus Layers-Florida Area Cirrus Experiment (CRYSTAL-FACE) [*Jensen et al*., 2004]; and the focus of the present study, the Tropical Composition, Cloud and Climate Coupling experiment (TC^4) [*Toon* summary paper, this collection, 2009]. In TC^4 the high altitude NASA ER-2 flew with the Solar Spectral Flux Radiometer (SSFR), which measured spectrally continuous solar irradiance, and the MODIS Airborne Simulator (MAS), a discrete-band imaging spectrometer that measured solar reflected radiance.

Simultaneous and co-located observations from these two instruments over tropical ice cloud layers helped to address several important questions regarding ice cloud radiative transfer: How well do current models of ice crystal single scattering properties reproduce the measured shortwave spectral albedo of ice clouds encountered during TC^4? Are systematic errors evident from the comparisons? How well do the retrieved values of optical thickness and effective radius retrieved from satellite-like measurements (MAS) reproduce the measured spectral albedo? Are there significant differences in ice retrievals between radiance-based and irradiance-based methods?

One of the main purposes of this study was to examine how well the models of single scattering optical properties of ice particles can reproduce the spectral albedo of ice clouds encountered during TC^4. Satellite retrievals of cloud optical thickness and effective radius are typically retrieved at just two spectral bands, one in the visible to very near-infrared where ice and liquid water are non-absorbing and the other in the shortwave -infrared where ice and liquid water weakly absorb. The former is most sensitive to cloud optical thickness, the latter to cloud particle size. For a complete description of this type of retrieval see, for example, *Twomey and Cocks* [1989] or *Nakajima and King* [1990].

Current models of ice single scattering properties contain far more than two wavelengths. The models used in this study contains 140-150 wavelengths [*Yang and Liou,* 1998; *Baum et al.*, 2005] spread across the solar spectrum. In principle, if the model of the single scattering is spectrally accurate, then the retrieved optical thickness and effective radius from as few as two wavelengths should accurately predict the spectral albedo for the entire spectrum. By retrieving the optical properties of ice clouds, using the classical two wavelength technique, one should be able to test, at the very least, how consistent the wavelength to wavelength albedo is modeled by comparing with spectral measurements of albedo from the SSFR.

The effects of cloud vertical [*Platnick*, 2000,] and horizontal [*Platnick*, 2001; *Eichler et al.*, 2009] inhomogeneity on the retrieval of cloud optical properties have been investigated previously. For clouds with varying vertical and or horizontal microphysical structure, the use of different wavelengths in the inversion procedures may result in different values of retrieved effective radius. However, these differences are typically small compared to retrieval errors. In this paper, all calculations were done for plane-parallel, homogenous (vertically and horizontally) clouds. The impact of vertical and/or horizontal cloud inhomogeneities on retrievals of optical thickness and effective radius was not investigated in this work.

Because many remote sensing retrievals of cloud optical thickness and effective radius rely on these single particle scattering models testing their spectral fidelity is an important validation. The accuracy of the models cannot be judged solely from remote sensing measurements as it implies some level of circularity. It would be preferable, for instance, to have an independent measurement of particle size. Particle size measurements, *in situ*, were made during TC^4, but are prone to crystal shattering [*McFarquhar et al.*, 2007; *Jensen et al*., 2009]. Even in the absence of *in situ* measurement errors like inlet shattering, issues of cloud volume sampling -small and usually deep within a cloud for *in situ* measurements-large and near cloud top for radiation measurements also confound efforts at comparing the two. For these reasons, no *in situ* data were used.

A previous study was conducted in a similar vein, comparing solar wavelengths with thermal wavelengths and found the two regions to have inconsistencies [*Baran and Francis,* 2004]. Here we have examined the spectral consistency at high spectral resolution and sampling over the majority of the solar spectrum, at optical thicknesses ranging from 3 to 46 and solar zenith angles ranging from 23^0 to 53^0. The differences between measured spectral albedo, and predicted spectral albedo derived from ice single scattering properties are discussed as are the differences in the retrieval from radiance and irradiance based measurements used in this study.

This paper is organized as follows: (1) the measurements of spectral irradiance from the SSFR and radiance imagery from MAS, (2) models of single scattering optical properties and their incorporation into a radiative transfer model along with the method employed for retrieving the optical thickness, effective radius, and albedo, (3) cloud optical thickness and effective radius retrieved from MAS radiance and SSFR irradiance using two currently available ice single scattering libraries, (4) the spectral albedo calculated from a two-wavelength SSFR retrieval compared with the measured spectral albedo and also the spectral albedo calculated from a two-wavelength MAS radiance retrieval compared with the measured spectral albedo, (5) individual spectra for high and low optical thickness and effective radius from each case, and (6) a summary of the work.

2. Measurements of Radiance and Irradiance during TC^4

The NASA ER-2 was instrumented with the SSFR and either the MAS [*King et al.,* 2004] or the MODIS/ASTER airborne simulator [*Hook et al*., 2001] for thirteen flights together over the course of the experiment. These flights covered a wide variety of cloud types, including extensive fields of low marine stratus, tropical convective systems, and high tropical ice clouds-the focus of this paper. The NASA DC-8 was also equipped with a SSFR, and coordinated flights with the ER-2 took place on several occasions, with the DC-8 flying below a cloud deck and the ER-2 above. Coordinated aircraft flight above and below a cloud layer enables the measurement of flux divergence or cloud absorption. This is the subject of a companion paper in this volume [*Schmidt* et al., 2009]. Here we focus solely on the reflected solar radiation at cloud top.

2.1 Solar Spectral Flux Radiometer (SSFR)

The SSFR consists of two spectroradiometers connected via a fiber optic to a miniature integrating sphere mounted on the top (zenith viewing) and bottom (nadir viewing) of the NASA ER-2. The integrating spheres provide the cosine response over the wide wavelength range of the SSFR that is required to make a measurement of spectral irradiance. The wavelength range of the instrument, 350 to 2150 nm, encompasses 90% of incident solar radiation. The spectral resolution as measured by the full-width-half-maximum (FWHM) of a line source is 8 nm from 400 to 1000 nm with 3 nm sampling and 12 FWHM from 1000 to 2200 nm with 4.5 nm sampling The SSFR records a nadir and zenith spectrum every second.

The spectrometers are calibrated in the laboratory with a NIST-traceable blackbody (tungsten-halogen 1000W bulb). The radiometric stability of the SSFR is carefully tracked during the course of a field experiment with a portable field calibration unit with a highly stable power source and 200W lamps. The calibration has generally held to the 1 to 2% level over the course of a several week field mission as it did during TC^4. The radiometric calibration was adjusted for minor fluctuations measured by the field calibration from flight to flight. In addition, the data were filtered using the aircraft navigation and ephemeris data to eliminate time periods when the aircraft attitude was not level (e.g. turns, takeoff and landing, turbulence). The estimated uncertainties in the absolute calibration of the instrument are 5%. We note that when retrieving cloud optical properties with albedos, as was done here, error in the absolute calibration cancel. Errors from unknown offsets in aircraft navigation data or reflections from clouds may remain however. For a more complete description of the SSFR instrument see [*Pilewskie et al*., 2003].

2.2 MODIS Airborne Simulator (MAS)

The MAS instrument is an imaging spectrometer with 50 discrete bands distributed throughout the solar reflected and thermal emitted parts of the spectrum. Twenty-two of the bands in the solar region overlap with the SSFR from 461 to 2213 nm. The spectral bandpass of MAS in the visible and near-infrared channels are in the range of 40-50 nm, it has a 2.5 mrad instantaneous field of view (IFOV), and 16-bit analog to digital conversion. MAS is typically pre- and post-flight calibrated in the laboratory with an integrating sphere and uses an integrating hemisphere in the field for stability monitoring. For details on MAS calibration issues and investigations during TC^4, see King et al., Because it is an imager, it provides excellent spatial context (~25 m nadir pixel resolution with ~17 km swath width for typical TC4 ice cloud heights) with which to help interpret the measurements of irradiance from SSFR.

All thirteen flights and all flight legs therein were examined with the MAS cloud product which includes cloud optical thickness, cloud phase, cloud top height, and temperature information. The flight legs used in this study were selected based on several criteria: the abundance of ice clouds; legs that were only over open ocean to simplify the input of surface spectral albedo into the radiative transfer calculations; the apparent absence of low level clouds which might make the retrieval of ice cloud properties more complicated and prone to error (an example of this which occurred frequently in the data are low level cumulus clouds, presumably liquid water, beneath an optically thin layer of ice cloud); and finally, stable, level flight which is required for the measurement of irradiance. Four flight tracks from 17 July 2007 met these criteria and were used for analysis in this work. The cosine of the mean solar zenith angles (denoted by μ) for the four flight legs were 0.60, 0.82, 0.88, and 0.92. For the remainder of this paper the four cases will be distinguished by their cosine of solar zenith angle. (i.e. the μ=0.82 case, the μ=0.88 case, etc). Of these cases three (μ=0.60, 0.82, 0.88) had low to moderate optical thickness (3-15) and one case (μ=0.92) had high optical thickness (40-50)

2.3 RadiativeTransfer Calculations of Irradiance

Analysis of solar spectral irradiance from SSFR has lead to the development of a radiative transfer code optimized for the spectral characteristics of the SSFR and for flexibility in specifying cloud and aerosol radiative properties [*Bergstrom et al.*, 2003; *Coddington et al.,* 2008] The molecular absorption by species such as water vapor, oxygen, ozone, and carbon dioxide, are calculated using the correlated-k method [*Lacis and Oinas*, 1991]. The band model was developed specifically for the SSFR by defining the spectral width of the bands by the slit function of the SSFR spectrometers, the half-widths of which were noted previously. The k-distribution is based on the HITRAN 2004 high resolution spectroscopic database [*Rothman et al.,* 2005]. The model uses the discrete ordinate radiative transfer method (DISORT) [*Stamnes et al.,* 1988] to solve for the spectral irradiance and nadir and zenith radiance at each level. Molecular scattering optical thickness is calculated using the analytical method of Bodhaine [*Bodhaine et al.,* 1999]. The model contains 36 levels. In this study albedo was calculated at 20 km, the nominal flight level of the ER-2. The albedo is defined as the ratio of upwelling to downwelling irradiance at the flight level. A standard tropical atmospheric profile of water vapor and well mixed radiatively active gases was used. No attempt was made to fit the water vapor amount to match the measurements; this would be computationally prohibitive and unnecessary, because the absorption bands of water vapor, oxygen, etc. are avoided for inferring cloud optical properties. Clouds heights for these cases were examined using the MAS cloud height product and were found to vary from between 8 to 12 km. A cloud height sensitivity test was performed by setting a cloud deck to 12 and to 8 km, for the retrieval of cloud optical properties. Little to no change in the retrieved values was found, so that the calculation was set to 10km for all of the cases. This is the result of using 870 nm as one of the retrieval wavelengths. The molecular scattering is reduced at this wavelength and the effect on the retrieval of cloud height was small. The use of a shorter wavelength (e.g. 500 nm) would likely show a greater sensitivity to cloud height.

The ice crystal single scattering models used here are the same ones used for the MODIS Collection 4 [*Baum et al*., 2000; *Platnick et al*., 2003; *Yang and Liou*, 1996; henceforth C4] and Collection 5 cloud products [*Baum et al*., 2005, henceforth C5]. The C5 models consist of plates, hollow and solid columns, 2-D bullet rosettes, and aggregates consisting of solid columns. These early models provide scattering properties for 5 size bins and were integrated over 12 particle size distributions. The C5 models consist of mixtures of different ice particle shapes (e.g. droxtals, solid and hollow columns, plates, 3-D bullet rosettes, and aggregates of columns). The scattering properties for each of these particles are available for 45 individual size bins. For both sets of bulk models, all particles are smooth except for the aggregate, which is roughened. Each size regime in the models consists of a different mixture; the smallest consists of only droxtals, and the largest is predominantly bullet rosettes. Intermediate sizes are varying mixtures of shapes.

The single scattering properties include a scattering phase function defined at 498 angles between 0^0 and 180^0, asymmetry parameter, extinction efficiency, extinction and scattering cross sections, single scattering albedo, and a delta transmission factor. The delta transmission factor is wavelength dependent and is used to scale the input optical thickness and single scattering albedo according to equations 1 and 2.

Eq. 1. $$\tau' = (1 - \delta\varpi_0)\tau$$

Eq. 2. $$\varpi_0' = \frac{(1-\delta)\varpi_0}{1-\delta\varpi_0}$$

where δ is the delta transmission factor, τ is the optical thickness, and ϖ_0 is the single-scattering albedo. The primed quantities are the δ-scaled values of optical thickness and single scattering albedo. The δ-transmission factor is used to account for transmission through plane parallel ice particle planes in the forward direction i.e. at a scattering angle of zero degrees [*Takano and Liou,* 1989]. The effective radius is defined by equation 3.

where <V> is the mean particle volume and <A> is the projected area for the ice crystal size distribution [*Mitchell,* 2002].

Eq. 3.
$$r_{eff} = \frac{3}{4}\frac{\langle V \rangle}{\langle A \rangle}$$

For C5 the ice particles range in size from 5 to 90 microns in a step size of ten microns for a total of eighteen different effective radii. The wavelength coverage is from 400 to 2200 nm, matching the SSFR coverage. The database contains some spectral gaps, in the regions 1000 -1200 nm, 1700 -1800 nm, and 1950-2050 nm. Outside of the gaps the spectral sampling is 10 nm. The results from an earlier library, C4, used in the MODIS collection 4 [*Platnick et al.,* 2003] are also shown. It has continuous spectral coverage from 400 to 1695 nm. The range of effective radii in C4 is 6.7 to 59 μm with a total of twelve effective radii. The small particles in C4 are assumed to be compact hexagonal ice particles, unlike the smallest particles in C5 which are assumed to be droxtals [*Yang et al.*, 2007]. The relative contribution of each particle shape to the size distribution is also different between C5 and C4; *Yang et al*. [2007] gives a detailed summary of each.

The input to the radiative transfer model first requires that the phase function be represented in terms of a Legendre polynomial series where the number of terms is set to the number of streams used in the DISORT calculation. All of the DISORT calculations for this study were done with 16 streams with Delta-M scaling [*Wiscombe,* 1977] to account for the strong forward scattering peak in the phase function typical of large size parameters. For the accurate calculation of irradiance at least six streams are required; streams are the number of quadrature points in the angular integration of scattering. We used the technique of *Hu et al.* [2000] to fit the phase function with the Legendre coefficients for input into the radiative transfer code.

The panel on the left hand side of Figure 1. shows an example of the library phase function at 870 nm for the largest (solid line) and smallest (dash-dot line) effective radii in C5. On the right hand panel of Figure 1 the single scattering albedo wavelength spectra of a smallest and largest size effective radii (C5) are shown. The phase function for the largest size exhibits ice halo features at 22 and 46 degrees; the phase function for the smallest particle size is notably smoother. In the shortwave-infrared the single scattering albedo for the largest size is reduced below that of the smallest size, as expected from simple geometric optics [*Bohren and Huffman,* 1983]. This forms the basis for the retrieval of effective radius in this spectral regime. Ice is essentially non-absorbing in the visible. No aerosol was included in the model as these are tropical, high level clouds, and are unlikely to contain much aerosol. The top of the atmosphere (TOA) solar spectrum is given by the Kurucz spectrum *Kurucz* [1992]. The surface albedo (always ocean) was specified by constant value of 0.03. To generate an albedo library for each case, a series of cloud optical thicknesses, thirty in total, were calculated for each of the four solar zenith angles. Optical thickness step sizes range from 0.5 at the smallest optical thickness, to 2 to 5, at intermediate optical thickness, and 10 at the highest optical thickness (50-100). The resolution in the calculation of the various effective radii was given by the single scattering ice library employed; eighteen in the case of the C5, twelve for the C4 library. The C4 library is not evenly spaced in effective radius; it contains finer sampling in the range of 25 to 40 μm. At this resolution, the spectra are sufficiently smooth so they can be interpolated with a high degree of accuracy to generate a finer optical thickness and effective radius grid. The optical thickness grid was linearly interpolated to increments of 0.1 from endpoints of the calculations, 0-100. The effective radii were linearly interpolated to a step size of 0.2 from the range of 5 to 90 μm in the C5 library and 6.7 μm to 59 μm in the C4 library. Figure 2 shows a range of optical thickness and effective radius of the calculated albedo spectra. The optical thicknesses are color coded and the effective radii are line style coded. Note that the spectra group by color in wavelengths between 400 and 1000 nm and contain information about optical thickness; the spectra cluster by line style for the wavelengths 1500 to 2150 nm, and contain information about effective radius.

3. Retrieval of optical thickness and effective radius from SSFR and MAS

For the retrieval of optical thickness and effective radius at least two wavelengths are chosen to determine a best fit to the calculated spectra. Previous work with retrievals from the SSFR has included up to five wavelengths [*Coddington et al.,* 2008]. Others have investigated the utility of including more than two wavelengths [*Cooper et al.*, 2006]. Because wavelength selection was not the focus of this study we have chosen to follow the technique used in satellite retrievals and use the MAS wavelengths 870nm (water non-absorbing) and 1600 nm or 2130 nm (water absorbing). Measurement to measurement variation was smaller at 1600 nm, so it was chosen for the water-absorbing wavelength applied in this analysis. A two step process was implemented as follows. The first step is an initial estimate from the uninterpolated data to determine the range that the measurement falls in; that range is used to constrain the retrieval in the interpolated data. This greatly increases the speed at which a minimum in the least squares fit is found, over the search of the entire high resolution library for each measurement. The "best-fit" is determined by minimizing the residual in a least squares sense (Equation 4), of the measurement to calculated albedo value at the given wavelengths.

Eq.4. $$residual = (vis_{measured} - vis_{\text{mod}\,led})^2 + (nir_{measured} - nir_{\text{mod}\,eled})^2$$

The calculation of optical thickness and effective radius for MAS is given by the MAS algorithm [*King et al*., 2004] and is identical for MODIS derived cloud optical properties. A separate retrieval of the MAS values of optical thickness and effective radius was not attempted in this work.

4. Analysis of spectral albedo properties

To test of the ability of single scattering models to accurately reproduce the observed spectral albedo, we retrieved the optical thickness and effective radius using SSFR albedo at two wavelengths from each spectrum coincident with the MAS flight legs. The retrieved optical thickness and effective radius were then used to calculate the entire spectrum with the radiative transfer model. The left-most plot in Figure 3a is the MAS 650 nm radiance for the μ=0.82 case; time (UTC) is along the y-axis, the cross-track swath of MAS along the x-axis. The second from the left, (3b) is the spectral albedo measured by the SSFR. Wavelengths varies along the x-axis, time is on the y-axis. Note the strong water vapor absorption in the measurements at 1400 nm and 1900 nm, and weaker bands at 1140 and 940 nm, all represented by vertical bands in the image. Figure 4 shows a typical SSFR albedo spectrum with the water vapor band centers and band widths shown to aid in interpreting the spectra. The third panel (Figure 3c) image is the spectral albedo reconstructed from the 2-wavelength SSFR retrieval of the cloud optical thickness and effective radius. The white bands are the aforementioned spectral gaps in the ice-crystal model data (C5). There is little evidence of water vapor absorption in this image. A comparison of the second and third panel images provides evidence that an insufficient amount of water vapor was used in the model but it is of no consequence in the present analysis because those bands were avoided in the retrievals. The image in the bottom panel shows the difference between the reconstructed albedo and the SSFR measured albedo. In this flight segment the optical thickness varied from 5 to 15 (see figure 9 for the time series) and the effective radius varied from 25 to 35 μm. The difference image varies little over this change in optical thickness and effective radius, indicating that the single scattering optical properties given in C5 capture the range of possible single scattering properties needed to accurately reproduce the spectral albedos that were encountered during the flights examined here. Indeed, the difference plots for the μ=0.88 and μ=0.60 cases (not shown) are virtually identical to the μ=0.82 case shown here. The μ=0.92 case is somewhat different as will be discussed later in the paper when examining individual spectra.

In general, the differences outside of strong molecular gaseous absorption bands (which has not been varied from a standard tropical profile and is highly variable for water vapor) falls within 0.05 of the measured albedo. All four cases examined here fall within moderate to high optical thicknesses. For the cloud optical thicknesses examined here, all substantially greater than unity, the spectral albedo is not sensitive to particle shape [*Wendisch et al.*, 2005]. Instead the effects of absorption are amplified through multiple scattering and the single scattering albedo becomes the important single scattering property for accurately reproducing the spectral shape of the albedo.

In Figure 5 the differences for all times are plotted at each wavelength showing the entire range of differences for all wavelengths (the small black dots that in aggregate form a line). Superimposed (red diamonds) is the calculated mean albedo difference at each wavelength. The albedo differences are typically less than 0.05, with some exception. Many of largest deviations occur on the edges of strong molecular absorbers such as the 1400 and 1900 nm water vapor wings or the strong oxygen band at 763 nm and are the result of gaseous absorption.

The μ=0.88 case is the most spatially uniform, albeit short in duration, of the flight legs examined here; it has the smallest retrieved range and standard deviation in optical thickness. In terms of determining systematic differences between model and measurement, this is perhaps the best of the flight legs because spatial homogeneity is greatest. Wavelength to wavelength consistency (spectral shape) is similar for all the cases, although the variation within a particular wavelength may be greater (μ=0.92) or lesser (μ=0.82). The differences at the shortest wavelengths could be explained by differences in molecular scattering and/or the presence of aerosols. Because these errors are typically less than 0.03, and close to measurement error, no further refinement of the modeling was undertaken.

The exception to this is the μ=0.92 that had optical thicknesses substantially higher (33-46) than the other cases (3-15). At the shortest wavelengths the differences are 0.07-0.08. The spectral shape of the differences is similar to the others cases, but the magnitude is greater. This is true only of the shorter wavelengths; for the wavelengths longer than 1500 nm the agreement is within 0.02-0.03. The reason for this difference is unresolved. The largest systematic difference between measurement and model in all cases, outside of strong gas absorption, occurs in the 1200 to 1300 nm range. Although this region does contain a relatively narrow collision band of oxygen at 1270 nm the mismatch is much broader. This mismatch increases with increasing optical thickness, and is most evident for the μ=0.92 case that has substantially higher optical thickness than the other cases. This may indicate that the single-scattering albedo is too high in this spectral region as multiple scattering (high optical thickness) amplifies absorption. The ice single-scattering properties in C4 and C5 used the *Warren* [1984] compilation for the ice optical constants. A new compilation by *Warren and Brandt* [2008] contains substantial changes in the near-infrared complex part of the index of refraction. These changes have been implemented in the most recent single-scattering ice calculations from the developers of C4 and C5, but were not available for this analysis.

A more detailed representation of the differences between the highest and lowest retrieved values of optical thickness and effective radius (four in total) for each of the four segments and its corresponding spectral albedo from SSFR is plotted in Figures 6 and 7. SSFR albedo spectra are plotted in black and are continuous; the red spectra were the reconstructed using C5, and the blue spectra C4. The regions of best agreement are from 1500 to 2100 nm, excluding the strong water vapor band at 1900mn. For the case μ=0.92, the high optical thickness and height of the cloud reduce the water vapor absorption to the point where it ceases to interfere with the cloud albedo. This is because the column water vapor above these high altitude clouds is low and the contribution of water vapor absorption from below the cloud layer (due to its high optical thickness) is small. In the lower optical thickness cases, we are seeing “through” the cloud layer and the contribution of water vapor absorption from below the cloud layer is much greater.

The agreement is quite similar (0.02) to the surrounding spectrum where water vapor does not interfere with the ice cloud albedo. Note that in all the cases, as the optical thickness becomes larger, the mismatch between the modeled and measured spectra becomes larger in the 1200-1300 nm spectral region.

The effective radii for the C5 based retrieval are smaller in general than those from C4. The optical thicknesses are generally greater for C5 than C4. This is in agreement with a comparison done for the MODIS 4 and MODIS 5 collections (based in part on C4 for MODIS 4 and C5 for MODIS 5) by *Yang et al.,* [2007] that showed average optical thickness is greater by 1.2 from C5 (MODIS 5 collection) and an average greater effective radius from C4 (MODIS 4 collection) of 1.8 μm.

5. Comparison of Irradiance and Radiance Derived Optical Properties

The comparison of irradiance measurements (SSFR) and radiance (MAS) is challenging for several reasons. Perhaps the greatest of these is the difference in spatial sampling of the cloud field. MAS measures radiance over a finite swath width, 37 km at the ground. The SSFR measures the cosine weighted radiance integrated over the upward and downward hemispheres centered at the aircraft. To compare measurements from the two instruments the MAS radiance is spatially averaged following the analysis of *Schmidt et al*. [2007]. The technique averages MAS radiance over the half power point of the SSFR signal. The diameter of the SSFR half power point is approximately the MAS swath width, 17 km for a cloud deck at 10km and an ER-2 altitude of 20 km. Figure 8 shows the retrieved MAS optical thickness and effective radius from μ=0.88. The circle overlying the left part of the image represents the half-power region of an SSFR measurement. For the times series of retrieved optical properties, Figure 8, the circle is stepped down the image by one scan line, and a new average is calculated. This time (flight) series of averages are compared for the two different instruments. Unlike the SSFR, which uses measured downward irradiance to calculate the albedo, the MAS-derived reflectance relies on absolute radiometric calibration and a top-of-atmosphere solar irradiance spectrum.

In Figure 9 times series of retrieved optical thickness and effective radius are shown for the four cases. For all cases, MAS optical thickness retrievals are greater than those from SSFR; conversely, effective radius retrieved by SSFR is nearly always greater. Because SSFR views an entire hemisphere, in nearly all cases this includes some unknown fraction of open water. This could explain the consistent bias of higher optical thickness retrieved by MAS relative to SSFR. In general these differences are small; the average difference is 2-3 in optical thickness and 2-3 μm in effective radius. For short periods of time the differences can reach up to 12. The largest absolute difference occurs in the high optical thickness case μ=0.92. As the optical thickness increases, the albedo approaches its asymptotic limit. This means that small changes in albedo or reflectance (or radiometric calibration) produce large changes in retrieved optical thickness. This is consistent with the finding here that the largest differences in optical thickness were found at relatively high values of optical thickness. A summary of the average differences between the irradiance- and radiance-based retrievals and their standard deviations is given in Table 1.

The variability of optical thickness and effective radius over a flight segment is higher for MAS, indicating that even after averaging the MAS values, the radiative smoothing from SSFR is greater still. This is not unexpected, as half the energy incident on the SSFR originates from outside the swath of MAS. In addition, because the effects of scattering are more pronounced at the shortest wavelengths (conservative scattering), the variation in retrieved optical thickness is greater due to a greater contribution to the signal from outside the view of MAS. Figure 10 shows the differences between measured spectral albedo from SSFR from modeled spectral albedo derived using the MAS-retrieved optical thickness and effective radius. The differences are greater than those derived from the 2-wavelength SSFR retrievals (Fig. 5). The bias in optical thickness retrieval produces a MAS-derived spectral albedo that is generally higher in the visible. For the moderately absorbing spectral region from 1500 to 2100 nm the differences are reduced and are generally within 0.05; for μ =0.88 case the differences are even lower, between 0.01-0.02. Condensed water is weakly absorbing at these wavelengths so scattering is reduced, resulting in smaller contributions from outside of the MAS swath and better agreement. This is likely scene dependent, with the presence or absence of clouds outside the MAS field of view also determining in part, the level of agreement.

In Figure 11, the SSFR and MAS retrievals of optical thickness and effective radius are compared for each case. The order is sequential in cosine of solar zenith angle: the top row is μ=0.60, the bottom row μ=0.92. The left column shows comparisons of retrieved optical thicknesses, the middle column the retrieved effective radii, and the right column ratios of the effective radii retrieved by SSFR to that retrieved by MAS plotted against the retrieved optical thickness from MAS. The plots of retrieved optical thicknesses show a bias of higher optical thickness retrieved from MAS; this bias increases as the optical thickness increases. This is most evident in the last row (μ=0.92) where the optical thicknesses are 3-4 times greater than those in the other three cases and deviation from the one to one line is substantial. The effective radius plots (center column), also indicate a bias, as was stated previously, of larger effective radii retrieved by SSFR. In the effective radii ratios versus optical thickness (right column), for optical thicknesses less than 20 the differences in effective radii are large, up to 50%, (excluding the brief departure of 200% in the μ=0.82 case which may be the result of underlying liquid water clouds). As the optical thickness increases the agreement in effective radius becomes better. This is true in every case, even the high optical thickness case (μ=0.92) which agrees to within 10% at an optical thickness of 60 and is within 5% at an optical thickness of 90. For all cases, the agreement is 10% or better when the optical thickness is 22 or greater. For low optical thickness, the influence of surface albedo (dark ocean) is greater, biasing the results to a larger effective radius. The MAS retrieval of cloud optical properties, because it is spatially resolved, rejects pixels that are cloud free. As optical thickness increases, in relatively planar ice clouds, the effects of cloud heterogeneity and surface albedo are less of a factor and the agreement becomes better. Despite the differences in the spatial averaging, and potential differences in radiometric calibration, the MAS retrievals reproduce the observed spectral albedo to within 0.10 across the entire spectrum. In the most spatially uniform case (μ=0.88) the differences are considerably smaller. A radiometric offset between SSFR and MAS would also contribute to the differences in the retrievals between the two instruments. Similar comparisons to those presented in this study could be made with MODIS coverage to provide a better spatial context with which to judge the total contribution of cloud to the SSFR signal but would be hampered by differences in temporal sampling. The coincidence of satellite, aircraft, and cloud conditions did not allow for such a comparison in this study.

6. Summary

Optical remote sensing of the microphysical and optical properties of ice clouds from satellites has focused on the retrieval of the two cloud properties necessary (but not always to completely specify the inputs into radiative transfer models to recreate the spectral albedo: cloud optical thickness and effective cloud particle radius. These retrievals ultimately rely on models of bulk ice cloud single scattering properties of ice particles to determine the values of optical thickness and effective radius. If the single scattering parameters are correct or at least spectrally consistent and the retrieval is robust, then the retrieval results can be used in radiative transfer models should correctly recreate the spectral albedo. In the first part of this paper, a test the C5 and C4 libraries of ice crystal single scattering properties was performed. The optical thickness and effective radius were retrieved using a two-wavelength fit similar to that used by satellites (MODIS) or its airborne proxy (MAS). The retrieved values were derived from the SSFR measurements to remove biases due to spatial sampling differences between SSFR and MAS. In addition, SSFR measures upwelling and downwelling irradiance, reducing the errors that might occur from absolute radiometric calibration errors, providing a more rigorous test of the model ice single scattering properties. The retrieved effective radius and optical thickness were subsequently used to predict the measured spectral albedo. The measured and modeled spectral albedo were found to be in very good agreement, especially for the longer wavelengths (1500-2100 nm) where the albedo differences were within 0.02-0.03 over the four flight segments, with a range in effective radius from 25 to 40 μm. The optical thicknesses showed larger differences, yet still produced differences between modeled and measured albedo spectra that were within 0.05. In general the disagreement was largest at shorter wavelengths, up to 0.09 for the high optical thickness case (μ=0.92) which may suggest a problem in the molecular scattering component of the modeling or, less likely, the presence of aerosols. Ice scattering properties may also be a source of error although at lower optical thickness the model and measurements agree quite well. It is difficult to draw a firm conclusion based on a single high optical thickness case. The greatest systematic discrepancy between the measurements and models was for the wavelength region between 1200 nm and 1300 nm. In the lowest optical thickness cases the agreement was consistent with adjacent spectral bands. As the optical thickness increased, the differences were more pronounced. In the highest optical thickness case, the albedo bias approached 0.10. The increasing error with increasing optical thickness may suggest that the model single-scattering albedo is too high in this spectral band. The increase in multiple scattering amplifies absorption and could lead to a discrepancy such as is seen here.

In the second part of this paper we examined the retrievals from MAS, a satellite-like sensor. The MAS retrievals of optical thickness and effective radius were used with the radiative transfer model to predict the spectral albedo. This is a more challenging task for two reasons: unlike the SSFR, the MAS instrument relies on its absolute radiometric calibration to accurately predict reflectance and to determine optical thickness and effective radius. It also measures radiance over a finite swath width, whereas SSFR measures irradiance over a hemisphere. This introduces spatial sampling differences which cannot be completely resolved. Nevertheless, averaging the derived optical properties over the half-power point of SSFR, reproduces the majority of spectral albedo to within 0.05 with the greatest differences occurring in the 400-1200 wavelength range where scattering is greatest and the differences in spatially sampling are exacerbated. For the longer wavelengths, greater than 1500 nm, the agreement is better, in the range of 0.03 or less. A comparison of the retrieved optical thickness and effective radius from SSFR and MAS shows an average absolute deviation of 2.76 in optical thickness and 2.24 μm in effective radius for the three cases of low to moderate optical thickness. The high optical thickness case shows a much greater difference of 40.5 in optical thickness and 1.3 μm in effective radius. At these high optical thicknesses, the retrieval (optical thickness value) is highly sensitive to small changes in radiance (irradiance) as albedo reaches its asymptotic limit. The differences are systematic between MAS and SSFR with MAS nearly always retrieving a higher optical thickness and SSFR nearly always retrieving a larger effective radius. This could be explained by a radiometric calibration error; small differences in the radiometric calibration would produce the largest changes in optical thickness when optical thickness is already high. Additionally, the SSFR hemispherical field of view nearly always includes some fraction of open water. This would also lead to SSFR retrieving a smaller optical thickness. Spatial sampling differences prevent any definitive answer to this discrepancy, and in any case, the overall effect is small when calculating spectral albedo.

The role of single scattering properties for ice crystals are crucial in satellite retrievals of ice cloud properties and ultimately for radiative transfer calculations and their inclusion in ice cloud modeling in climate models We have examined here the spectral consistency of these properties within the solar spectrum and over a range of solar zenith angles and optical thicknesses encountered during TC^4. We have validated the fidelity of the derived properties of optical thickness and effective radius based on ice single scattering properties to recreate the spectral albedo when used in a radiative transfer model. New models from the same authors of the single scattering properties used here have been developed for ice crystals with varying surface morphologies, from smooth to rough and substantially roughened ice crystals. These models will have continuous spectral sampling over the range of the SSFR instrument. They also include updated values for the ice optical constants, which have changed substantially in the near-infrared [*Baum,* 2009 personal communication]. These new libraries will be compared with the same cases shown here to determine their ability to accurately reproduce spectral albedo and to examine the impact on the retrieval of ice cloud optical properties.

Acknowledgments

Bryan Baum acknowledges support through a NASA grant (NNX08AF81G).

References

Baran, A. J. (2004), On the scattering and absorption properties of cirrus cloud, *J. Quant. Spectrosc. Radiat. Transfer, 89*, 17-36.

Baran, A. J., and P. N. Francis (2004), On the radiative properties of cirrus cloud at solar and thermal wavelengths: A test of model consistency using high-resolution airborne radiance measurements, *Q. J. R. Meteorol. Soc.*, 130, 763-778, doi:10.1256/qj.03.151.

Baran, A. J., and S. Havemann (2004), The dependence of retrieved cirrus ice-crystal effective dimension on assumed ice-crystal geometry and size-distribution function at solar wavelengths, *Q. J. R. Meteorol. Soc., 130*, 2153-2167, doi:10.1256/qj.03.154.

Baran, A., P. Watts, and P. Francis (1999), Testing the coherence of cirrus microphysical and bulk properties retrieved from dual-viewing multispectral satellite radiance measurements, *J. Geophys. Res., 104*(D24), 31673-31683.

Baran, A. J., P. N. Francis, L.-C. Labonnote, and M. Doutriaux-Boucher (2001), A scattering phase function for ice cloud: Tests of applicability using aircraft and satellite multi-angle multi-wavelength radiance measurements of cirrus, *Q. J. R. Meteorol. Soc., 127,* 2395-2416, doi:10.1002/qj.49712757711.

Baran, A. J., S. Havemann, P. N. Francis, and P. D. Watts (2003), A consistent set of single-scattering properties for cirrus cloud: tests using radiance measurements from a dual-viewing multi-wavelength satellite-based instrument, *J. Quant. Spectrosc. Radiat. Transfer, 79*, 549-567.

Baum, B. A., D. P. Kratz, P. Yang, S. C. Out Y. Hu, P. F. Soulen, and S. C. Tsay, (2000), Remote sensing of cloud properties using MODIS airborne simulator imagery during SUCCESS, 1, data and models, *J. Geophys. Res., 105,* 11781-11792

Baum, B. A., P. Yang, A. J. Heymsfield, S. Platnick, M. D. King, Y.-X. Hu, and S. T. Bedka (2005), Bulk Scattering Properties for the Remote Sensing of Ice Clouds. Part II: Narrowband Models, *Journal of Applied Meteorology*, *44*, 1896–1911, doi:10.1175/JAM2309.1.

Bergstrom, R. W., P. Pilewskie, B. Schmid, and P. B. Russell (2003), Estimates of the spectral aerosol single scattering albedo and aerosol radiative effects during SAFARI 2000, *J. Geophys. Res., 108(D13)*, 8474, doi:10.1029/2002JD002435.

Bodhaine, B. A., N. B. Wood, E. G. Dutton, and J. R. Slusser (1999), On Rayleigh Optical Depth Calculations, *J. Atmos. Oceanic. Technol.*, 16, 1854– 1861.

Bohren C. F., and D. R. Huffman (1983) *Absorption and Scattering of Light by Small Particles*, Wiley-Interscience.

Chen, T., W. B. Rossow, and Y. C. Zhang (2000), Radiative effects of cloud-type variations, *J. Clim., 13*(1), 264-286,doi:101175/1520-0442(2000)013<0264:REOCTV.2.0.CO;2.

Coddington, O., K. S. Schmidt, P. Pilewskie, W. J. Gore, R. W. Bergstrom, M. Roman, J. Redemann, P. B. Russell, J. Liu, and C. C. Schaaf (2008), Aircraft measurements of spectral surface albedo and its consistency with ground-based and space-borne observations, *J. Geophys. Res., 113,* D17209, doi:10.1029/2008JD010089.

Cooper, S. J., T. S. L'Ecuyer, P. Gabriel, A. J. Baran, and G. L. Stephens (2006), Objective Assessment of the Information Content of Visible and Infrared Radiance Measurements for Cloud Microphysical Property Retrievals over the Global Oceans. Part II: Ice Clouds, *Journal of Applied Meteorology and Climatology, 45*, 42–62, doi:10.1175/JAM2327.1.

Ebert, E. E., and J. A. Curry (1992), A parameterization of ice cloud optical properties for climate models, *J. Geophys. Res., 97, (D4),* 3831-3836

Eichler, H., K. S. Schmidt, R. Buras, M. Wendisch, B. Mayer, P. Pilewskie, M. King, L. Tian, G. Heymsfield, S. Platnick (2009), Cirrus spatial heterogeneity and ice crystal shape: Effects on remote sensing of cirrus optical thickness and effective crystal radius, submitted to *J. Geophys. Res.*, this issue.

Hook, S. J., Thome, K. J., Fitzgerald, M., and A. B. Kahle, (2001), The MODIS/ASTER airborne simulator (MASTER) – a new instrument for earth science studies. *Rem. Sens. Envrn, 76*, 93-102

Hu, X-Y., B. Wielicki, B. Lin, G. Gibson, S.-C.Tsay, K. Stamnes and T. Wong (2000), □̃Fit: A fast and accurate treatment of particle scattering phase functions with weighted singular-value decomposition least-squares fitting. *J. Quant. Spectrosc. Radiat. Transfer, 65*, 681-690.

Jensen, E. J., and O. B. Toon (1994), Tropical cirrus cloud radiative forcing: Sensitivity studies, *Geophys Res Lett.*, *21*(18), 2023-2026.

Jensen, E. J., D. Starr, and O. B. Toon (2004), Mission investigates tropical cirrus clouds, *Eos Trans. AGU, 85*, 45-49

Jensen, E. J., et al. (2009), On the Importance of Small Ice Crystals in Tropical Anvil Cirrus. *Atmos. Chem. Phys. Discussion, 9*, 5321-5370.

Jiang, J. H., H. Su, S. T. Massie, P. Calarlo, M. Schoeberl, and S. Platnick (2009) Aerosol-CO relationship and aerosol effect on ice cloud particle size: Analyses from Aura MLS and Aqua MODIS observations. *J Geophys. Res*. (accepted).

King, M.D., Y. J. Kaufman, W. P. Menzel, and D. Tanre (1992), Remote sensing of cloud, aerosol, and water vapor properties from the moderate resolution imaging spectrometer (MODIS), *IEEE Trans. Geosci. Remote Sens., 30*, 2-27, doi:10.1109/36.124212.

King, M. D., S. C. Tsay, S. E. Platnick, M. Wang, and K. N. Liou, (1997) Cloud retrieval algorithms for MODIS: Optical thickness, effective particle radius, and thermodynamic phase, *MODIS Algorithm Theoretical Basis Document No. ATBD-MOD-05,*79pp [Online]. Available: modis-atmos.gsfc.nasa.gov/_docs/atbd_mod5.pdf.

King, M. D., S. Platnick, P. Yang, G. T. Arnold, M. A. Gray, J. C. Riedi, S. A. Ackerman, K. N. Liou (2004), Remote sensing of liquid water and ice cloud optical thickness and effective radius in the Arctic: Application of airborne multispectral MAS data*, J. Atmos. Oceanic Technol.*, *21* (6), 857–875.

Kurucz, R. L. (1992), Synthetic Infrared Spectra, in *Infrared solar physics: proceedings of the 154th Symposium of the International Astronomical Union,* edited by D. M. Rabin, J. T. Jefferies, and C. Lindsey, Kluwer Academic Publishers, Dordrecht, the Netherlands, 523-531.

Lacis, A. A., and V. Oinas (1991), A description of the correlated-k distribution method for modeling nongray gaseous absorption, thermal emission, and multiple scattering in vertically inhomogeneous atmospheres. *J. Geophys. Res 96,* 9027-9063

Macke, A., J. Muller, and E. Raschke, Single scattering properties of atmospheric crystals, *J. Atmos. Sci.*, 53, 2813-2825, 1996

McFarquhar, G. M., and A. J. Heymsfield (1998), The Definition and Significance of an Effective Radius for Ice Clouds, *J. Atmos. Sci., 55*, 2039-2052.

McFarquhar, G. M., J. Um, M. Freer, D. Baumgardner, G.L. Kok, and G. Mace (2007), Importance of small ice crystals to cirrus properties: Observations from the Tropical Warm Pool International Cloud Experiment (TWP-ICE). *Geophy Res Lett., 34,* L13803, doi:10.1029/2007GL029865

Mishchenko, M., W. Rossow, A. Macke, and A. Lacis (1996), Sensitivity of cirrus cloud albedo, bidirectional reflectance and optical thickness retrieval accuracy to ice particle shape, *J. Geophys. Res., 101*(D12), 16973-16985.

Mitchell, D. L. (2002), Effective Diameter in Radiation Transfer: General Definition, Applications, and Limitations, *J. Atmos. Sci., 59*, 2330-2346.

Nakajima, T., and M. D. King (1990), Determination of the Optical Thickness and Effective Particle Radius of Clouds from Reflected Solar Radiation Measurements. Part I: Theory, *Journal of the Atmospheric Sciences*, *47*, 1878–1893, doi:10.1175/1520-0469.

Pilewskie, P., J. Pommier, R. Bergstrom, W. Gore, S. Howard, M. Rabbette, B. Schmid, P. V. Hobbs, and S. C. Tsay (2003), Solar spectral radiative forcing during the Southern African Regional Science Initiative, *J. Geophys. Res.*, 108(D13), 8486, doi:10.1029/2002JD002411.

Platnick, S., (2000), Vertical photon transport in cloud remote sensing problems, *J. Geophys. Res.*, *105*(D18), 22919-22935.

Platnick., S., (2001), Approximations for horizontal photon transport in cloud remote sensing problems, *J. Quant. Spectrosc. Radiat. Transfer,68,* 75-99

Platnick, S., M. D. King, S. A. Ackerman, W. P. Menzel, B. A. Baum, J. C. Riedi, and R. A. Frey (2003), The MODIS cloud products: algorithms and examples from Terra, *IEEE Transactions on Geoscience and Remote Sensing, 41*, 459-473, doi:10.1109/TGRS.2002.808301.

Ramanathan, V., R. D. Cess, E. F. Harrison, P. Minnis, B. R. Barkstrom, E. Ahmad, and D. Hartmann (1989), Cloud-radiative forcing and climate—Results from the Earth Radiation Budget Experiment, *Science*, 243(4887), 57-63, doi:10.1126/science.243.4887.57.

Rothman., L., et al. (2005), The HITRAN 2004 molecular spectroscopic database. *J. Quant. Spectrosc. Radiat. Transfer, 96*, 139-204.

Schmidt, K. S., P. Pilewskie, S. Platnick, G. Wind, P. Yang, and M. Wendisch (2007), Comparing irradiance fields derived from Moderate Resolution Imaging Spectroradiometer airborne simulator cirrus cloud retrievals with solar spectral flux radiometer measurements, *J.Geophys. Res., 112*, D24206, doi:10.1029/2007JD008711.

Stamnes, K., S.-C. Tsay, W. Wiscombe, and K. Jayaweera (1988), Numerically stable algorithm for discrete-ordinate-method radiative transfer in multiple scattering and emitting layered media, *Applied Optics, 27*, 2502-2509.

Stephens, G. L., S.-C. Tsay, P. W. Stackhouse Jr., and P. J. Flatau (1990), The Relevance of the Microphysical and Radiative Properties of Cirrus Clouds to Climate and Climatic Feedback, *J. Atmos. Sci., 47*, 1742-1735.

Takano, Y., and K.N. Liou (1989), Solar Radiative Transfer in Cirrus Clouds. Part I: Single-Scattering and Optical Properties of Hexagonal Ice Crystals, *J. Atmos. Sci., 46*, 3-19.

Toon, O. B., D. Starr, E. Jensen, Jucks, M. Kurylo, H. Maring, P. Newman, S. Platnick, M. Schoeberl, P. Wennberg, and Wofsy (2009), The planning and execution of TC^4, submitted to *J. Geophys. Res.*, this issue.

Twomey, S., and T. Cocks (1982), Spectral reflectance of clouds in the near-infrared: Comparison of measurements and calculations, *J. Meteorol. Soc. Jpn. 60*, 583-592.

Waliser, D. E., et. al., (2009), Cloud ice: A climate model challenge with signs and expectations of progress, *J. Geophys. Res. 114*, D00A21, doi:10.1029/2008JD010015.

Warren, S. G., (1984), Optical constants of ice from the ultraviolet to the microwave, *Appl. Opt., 23,* 1206-1225.

Warren, S. G., and R. E. Brandt (2008), Optical constants of ice from the ultraviolet to the microwave: A revised compilation. *J. Geophys. Res., 113,* D14220, doi:10.1029/2007/JD009744

Wendisch, M., P. Pilewskie, J. Pommier, S. Howard, P. Yang, A. J. Heymsfield, C. G. Schmitt, D. Baumgardner, and B. Mayer (2005), Impact of cirrus crystal shape on solar spectral irradiance: A case study for subtropical cirrus, *J. Geophys. Res., 110*, D03202, doi:10.1029/2004JD005294.

Wiscombe, W. (1977) The delta-M method: rapid yet accurate radiative flux calculation for strongly asymmetric phase functions. *J. Atmos. Sci., 34,* 1408-1422.

Yang, P., and K. N. Liou (1998), Single-scattering properties of complex ice crystals in terrestrial atmosphere, *Contributions to Atmospheric Physics, 71*, 223-248.

Yang, P., B. A. Baum, A. J. Heymsfield, Y. X. Hu, H.-L. Huang, S.-C. Tsay, and S. Ackerman (2003), Single-scattering properties of droxtals, *J. Quant. Spectrosc. Radiat. Transfer, 79*, 1159-1169.

Yang, P., K. Liou, and W. Arnott (1997), Extinction efficiency and single-scattering albedo for laboratory and natural cirrus clouds, *J. Geophys. Res., 102*(D18), 21825-21835.

Yang, P., L. Zhang, S.L. Nasiri, B. A. Baum, H-L, Huang, M.D. King and S. Platnick (2007), Differences between collection 4 and 5 MODIS ice cloud optical/microphysical products and their impact on radiative forcing simulations. *IEEE Transactions on Geoscience and Remote Sensing, 45*, 2886-2899,

Table 1. Summary of optical thickness and effective radius for the four cases.

(μ)	MAS Optical Thickness [mean (standard deviation)]	MAS Effective Radius [mean (standard deviation)]	SSFR Optical Thickness [mean (standard deviation)]	SSFR Effective Radius [mean (standard deviation)]	Optical Thickness Difference (SSFR-MAS) [mean (standard deviation)]	Effective Radius Difference [mean (standard deviation)] (μm)
0.60	8.29(4.39)	27.95(4.05)	5.63(2.02)	30.43(2.53)	-2.67(2.55)	2.48(2.50)
0.82	12.49(5.53)	27.53(4.55)	7.64(2.47)	35.24(3.26)	-4.85(3.32)	7.71(3.11)
0.88	12.92(2.96)	35.74(0.63)	10.19(2.07)	36.93(0.63)	-2.73(1.07)	1.19(0.43)
0.92	80.42(7.47)	26.63(0.89)	39.92(2.65)	27.91(0.70)	-40.48(1.30)	1.28(0.07)

List of Figures

Figure 1. On the left are the phase functions at 870 nm from the C5 library for the largest 90 μm (solid line) and smallest 10 μm (dash-dot line) effective radii. On the right are again the largest (solid line) and smallest (dash-dot line) effective radii single-scattering albedo spectra.

Figure 2. The results of the C5 library in the radiative transfer calculations of albedo spectra for three different effective radii and four different optical thicknesses. The spectra cluster by color (optical thickness) in the 400-1000 nm wavelength range, and by line style (effective radius) in the 1500-2150 nm wavelength range.

Figure 3. 2-D representations of the μ=0.82 case. The first panel is MAS radiance at 650nm, the second panel is SSFR measured albedo, with wavelength on the x-axis, the third is the recreated albedo using optical thickness and effective radius retrieved from SSFR, and the last panel is a difference image.

Figure 4. A typical SSFR cloud albedo spectrum is shown with the major water vapor band centers (940, 1140, 1400 and 1900 nm) are overplotted with a vertical line. The approximate band widths are the shaded regions bounded by the dashed lines.

Figure 5. For each of the four cases,the difference between modeled and measured albedo, as parameterized by SSFR is shown. The black dots which aggregate to form lines, are the differences for every line in the MAS flight track, the red diamond is the mean difference.

Figure 6. For each case, the highest and lowest optical thickness and effective radius albedo spectrum is plotted with the full wavelength spectrum as predicted from the single scattering properties from C5 (red) and C4 (blue). Note the excellent agreement in all cases in the longer wavelength. As the optical thickness increases, the agreement becomes worse in the shorter wavelengths and the 1200-1300 nm range.

Figure 7. Same as figure. 6 but for the cases μ=0.88 and μ=0.92

Figure 8. The MAS retrieval of optical thickness and effective radius are shown (μ=0.88) with the SSFR half-power point (circle) over plotted.

Figure 9. The times series of optical thickness and effective radius retrieved by SSFR (black) and MAS (red) are shown for the four cases.

Figure 10. For each of the four cases, the difference between modeled and measured albedo, as parameterized by MAS is shown. The black dots are the differences for every line in the MAS flight track, the red diamond is the mean difference.

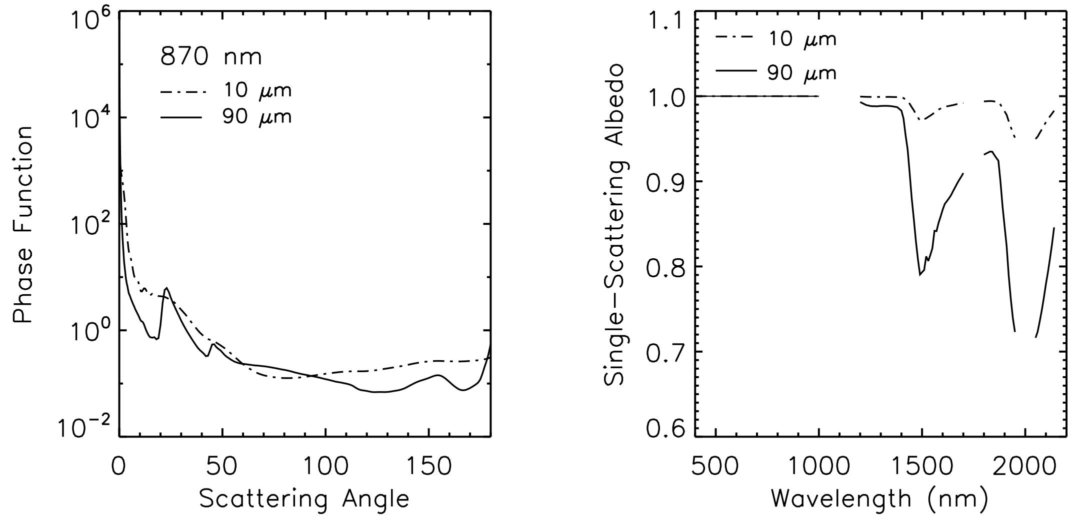

Figure 1. On the left are the phase functions at 870 nm from the C5 library for the largest 90 μm (solid line) and smallest 10 μm (dash-dot line) effective radii. On the right are again the largest (solid line) and smallest (dash-dot line) effective radii single-scattering albedo spectra.

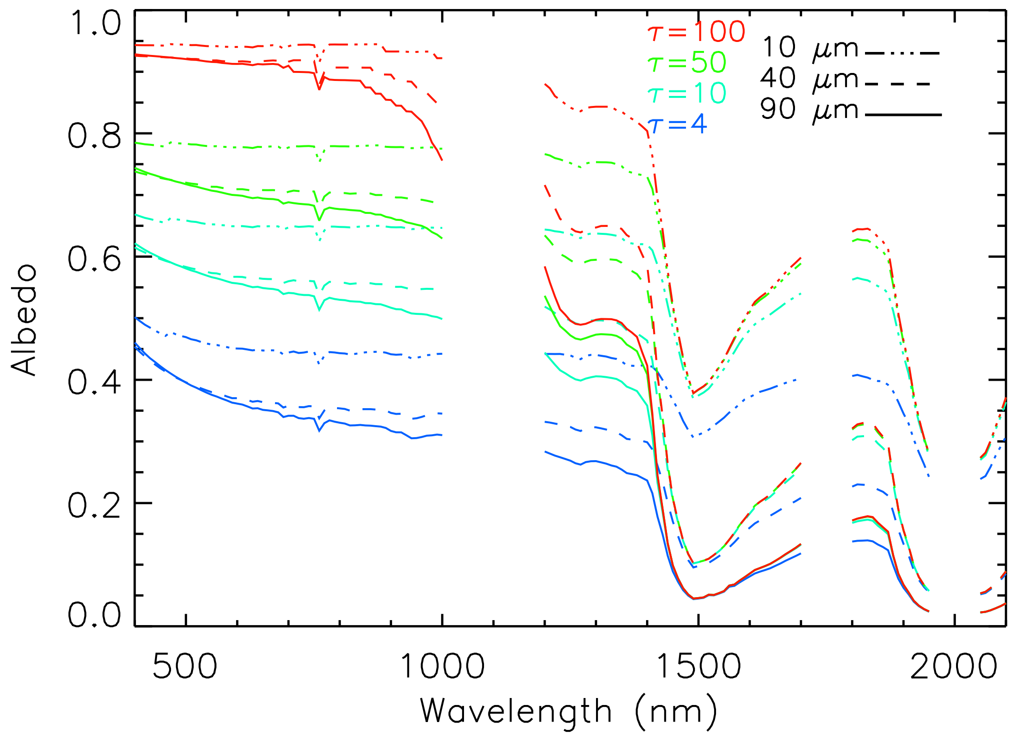

Figure 2. The results of the C5 library in the radiative transfer calculations of albedo spectra for three different effective radii and four different optical thicknesses. The spectra cluster by color (optical thickness) in the 400-1000 nm wavelength range, and by line style (effective radius) in the 1500-2150 nm wavelength range.

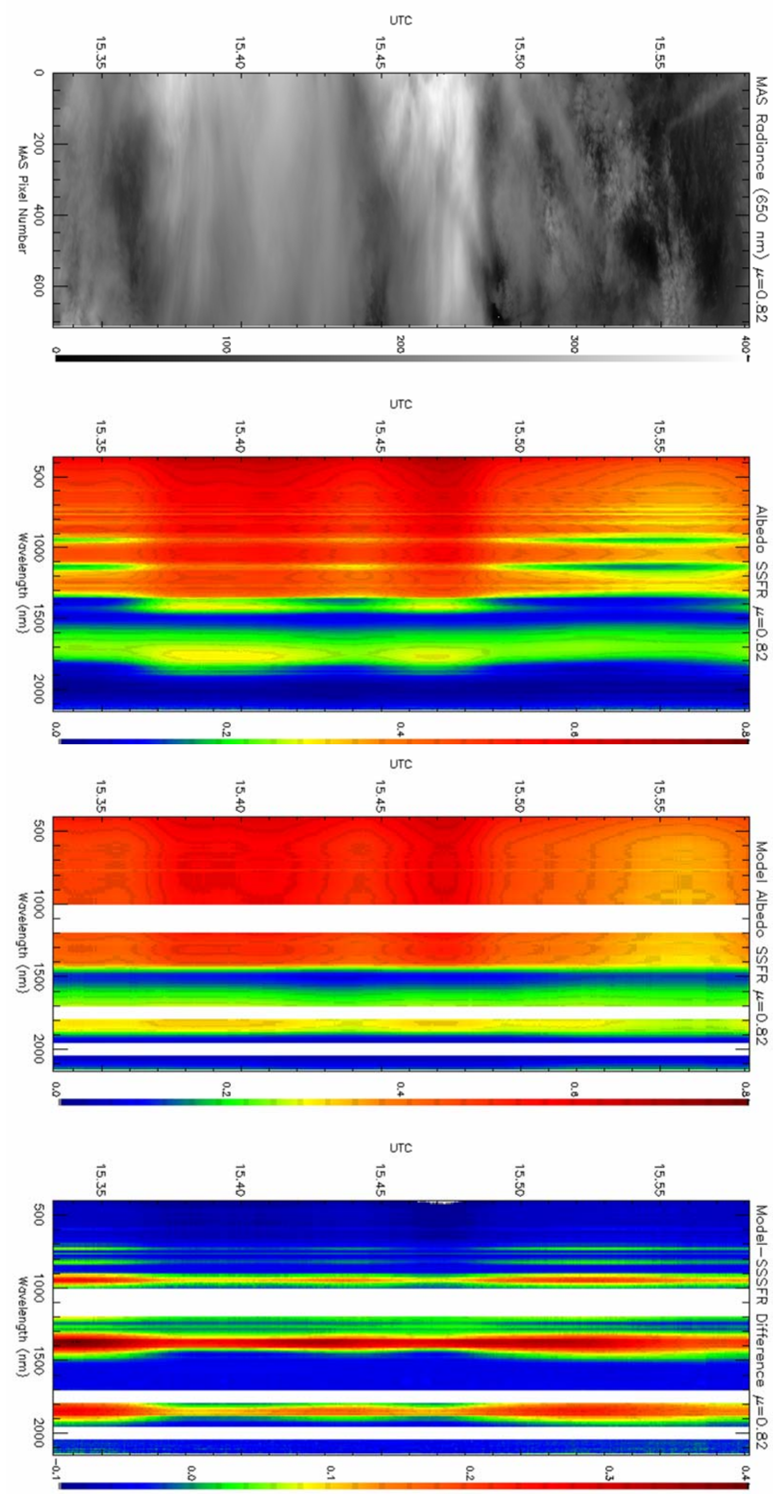

Figure 3. 2-D representations of the μ=0.82 case. The first panel is MAS radiance at 650nm, the second panel is SSFR measured albedo, with wavelength on the x-axis, the third is the recreated albedo using optical thickness and effective radius retrieved from SSFR, and the last panel is a difference image.

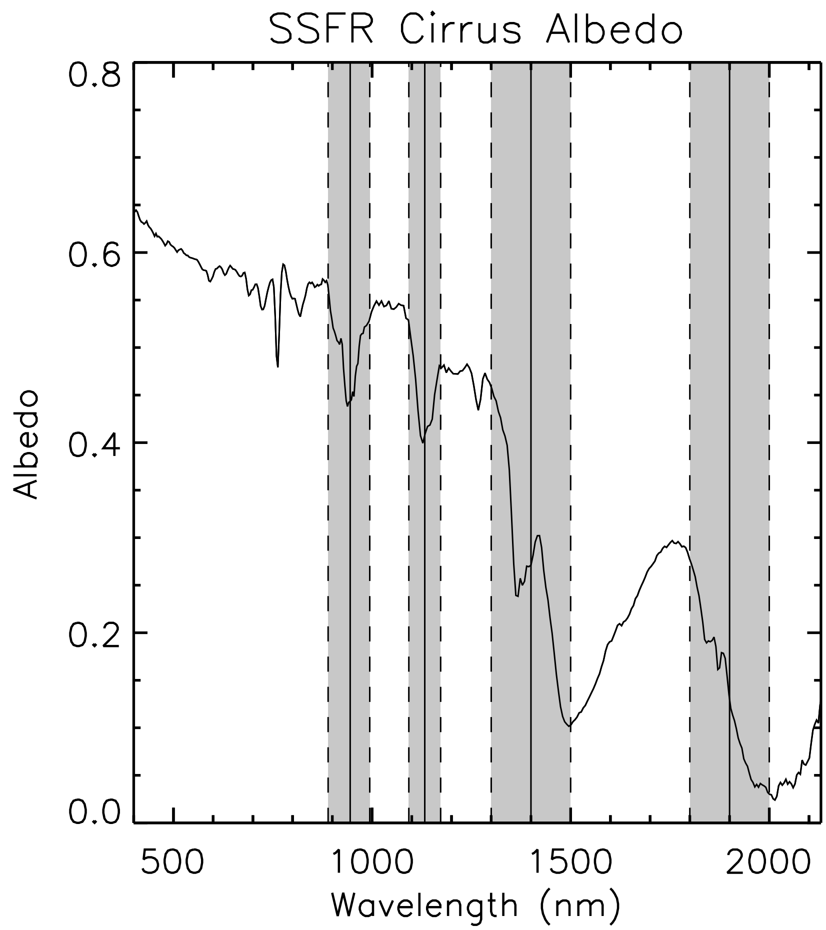

Figure 4. A typical SSFR cloud albedo spectrum is shown with the major water vapor band centers (940, 1140, 1400 and 1900 nm) are overplotted with a vertical line. The approximate band widths are the shaded regions bounded by the dashed lines.

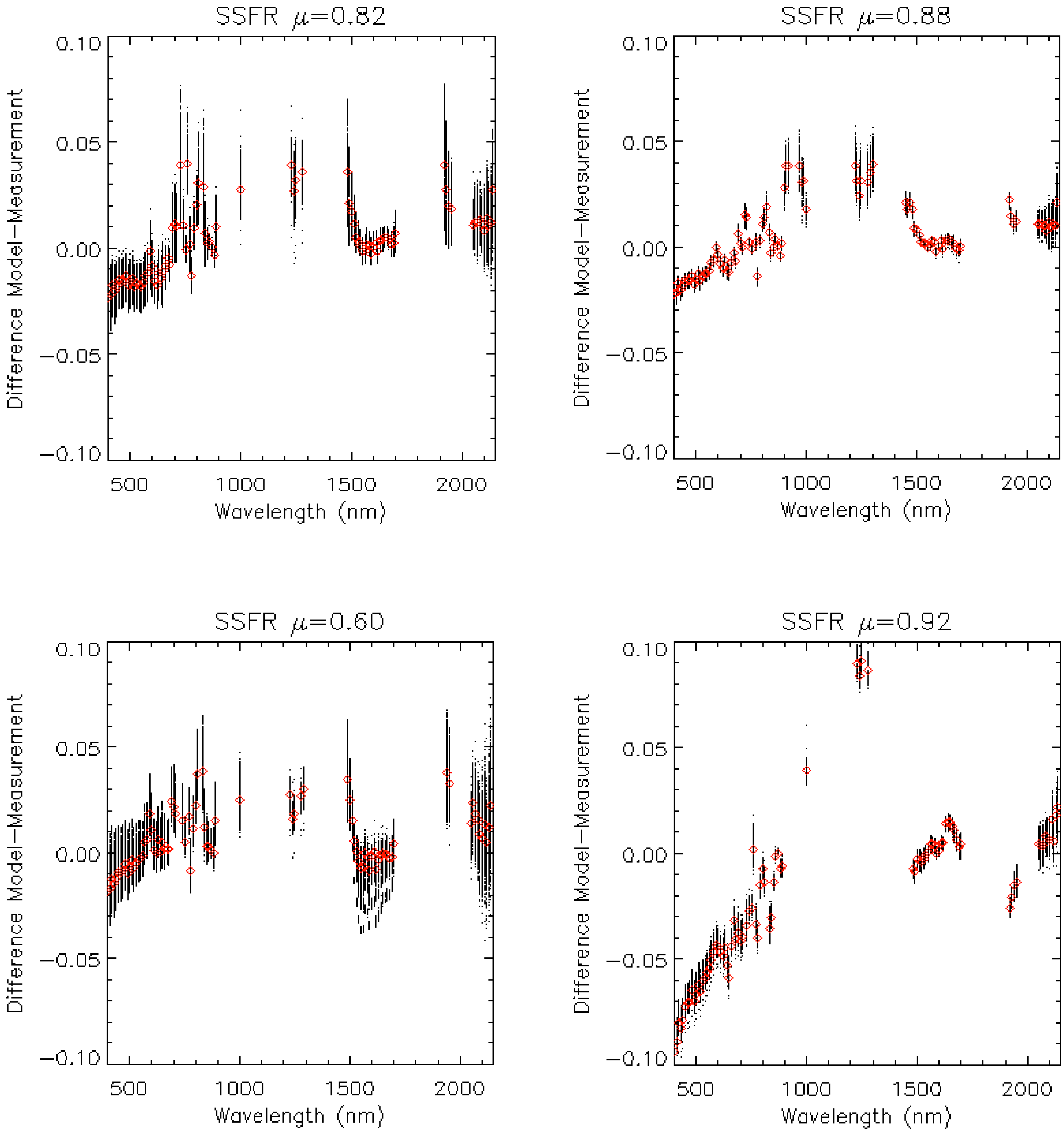

Figure 5. For each of the four cases,the difference between modeled and measured albedo, as parameterized by SSFR is shown. The black dots which aggregate to form lines, are the differences for every line in the MAS flight track, the red diamond is the mean difference.

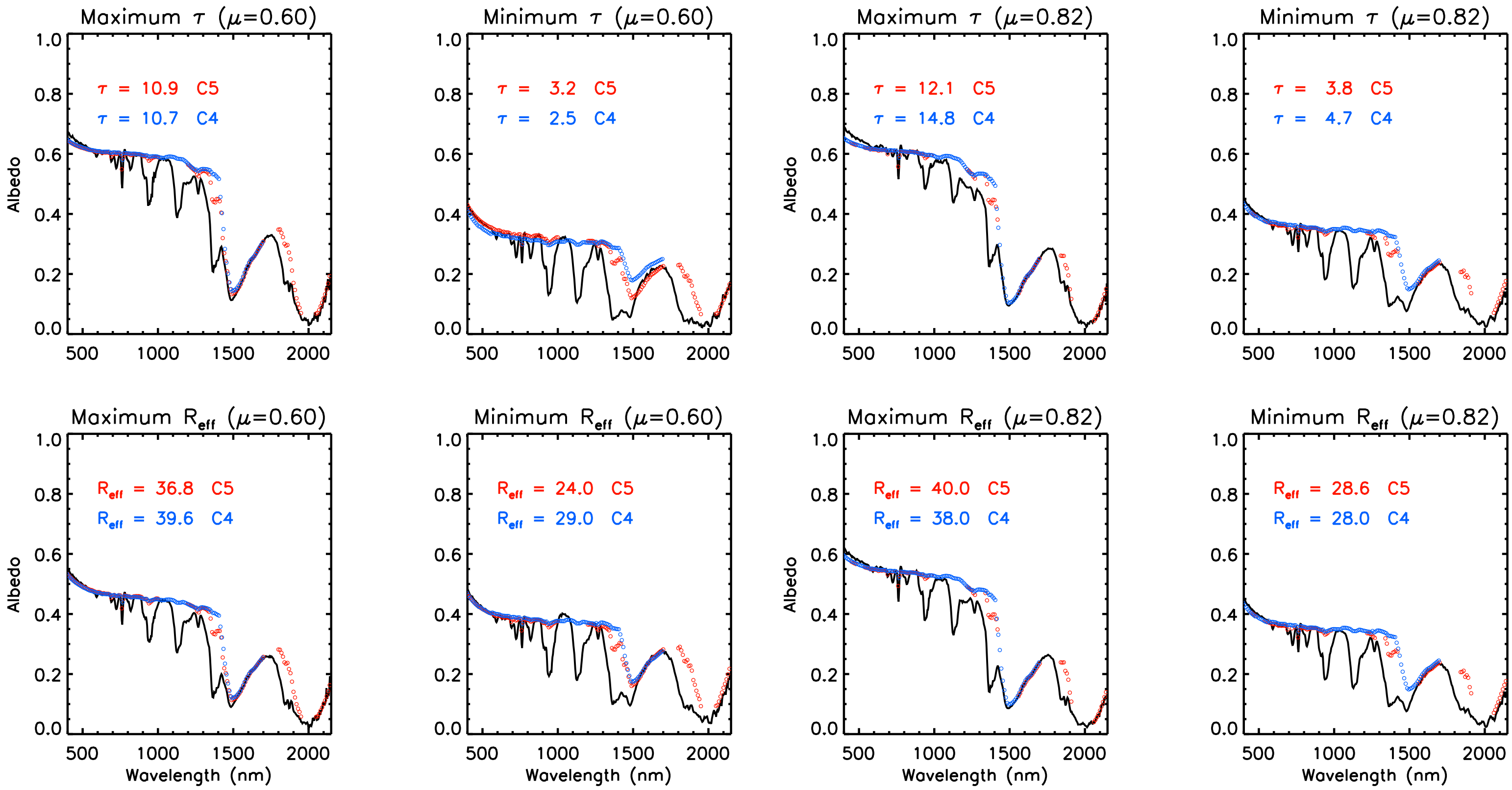

Figures 6. For each case, the highest and lowest optical thickness and effective radius albedo spectrum is plotted with the full wavelength spectrum as predicted from the single scattering properties from C5 (red) and C4 (blue). Note the excellent agreement in all cases in the longer wavelength. As the optical thickness increases, the agreement becomes worse in the shorter wavelengths and the 1200-1300nm range.

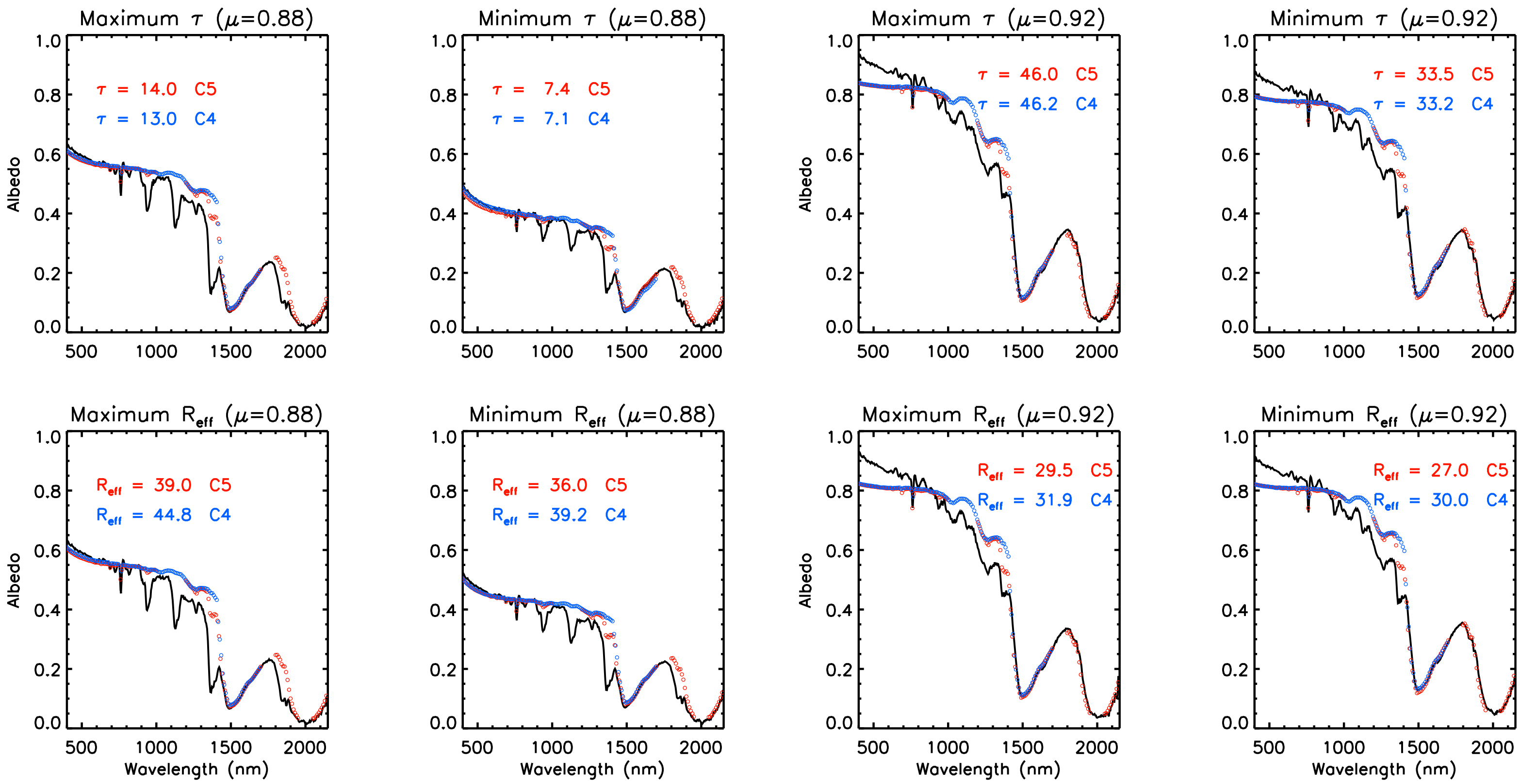

Figure 7. Same as figure 6 but for the cases μ=0.88 and μ=0.92.

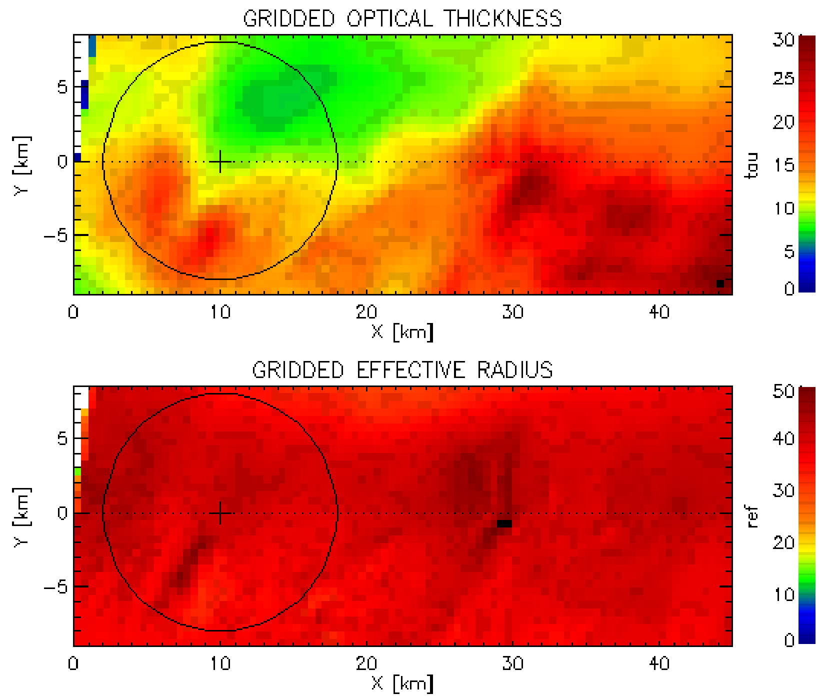

Figure 8. The MAS retrieval of optical thickness and effective radius are shown (μ=0.88) with the SSFR half-power point (circle) over plotted.

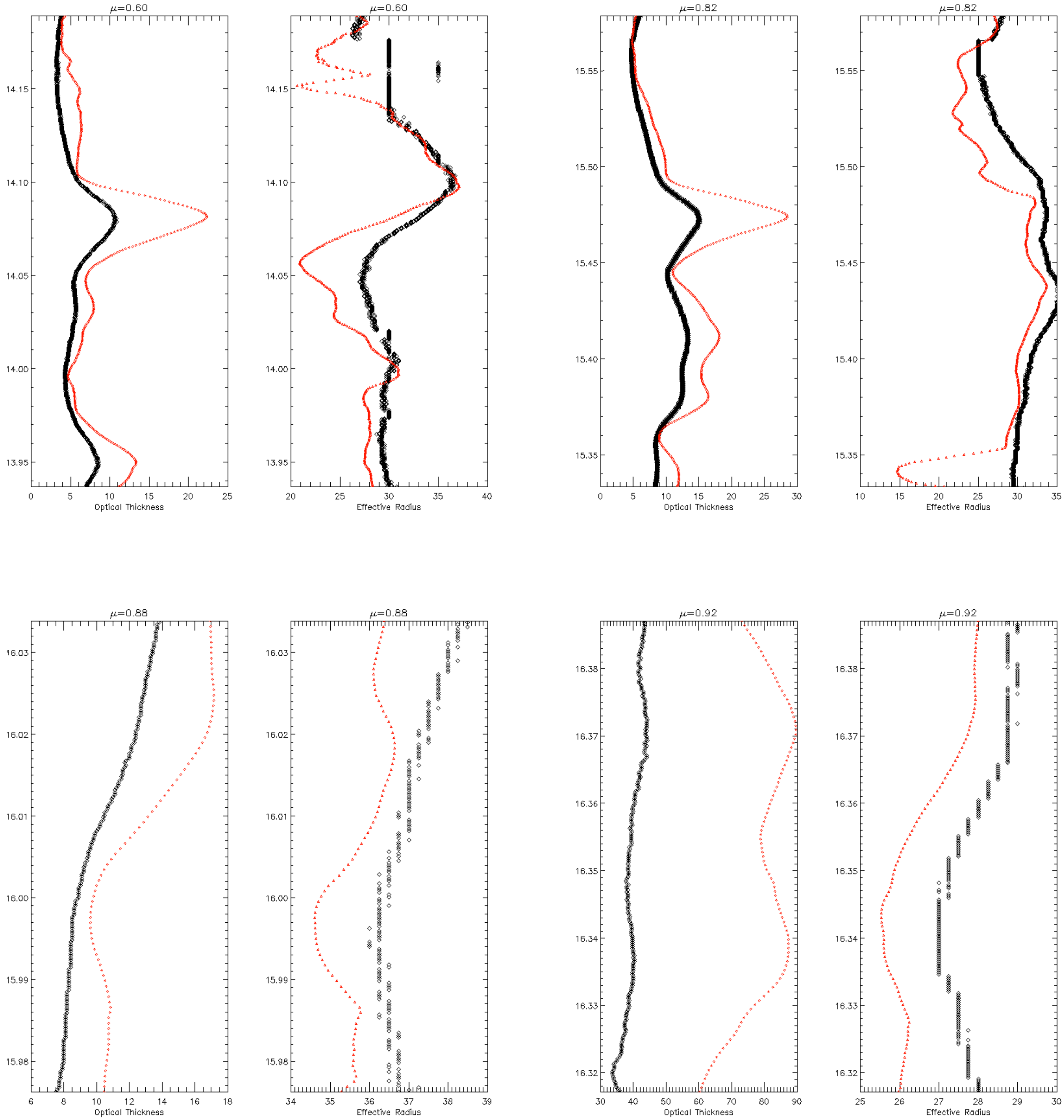

Figure 9. The times series of optical thickness and effective radius retrieved by SSFR (black) and MAS (red) are shown for the four cases.

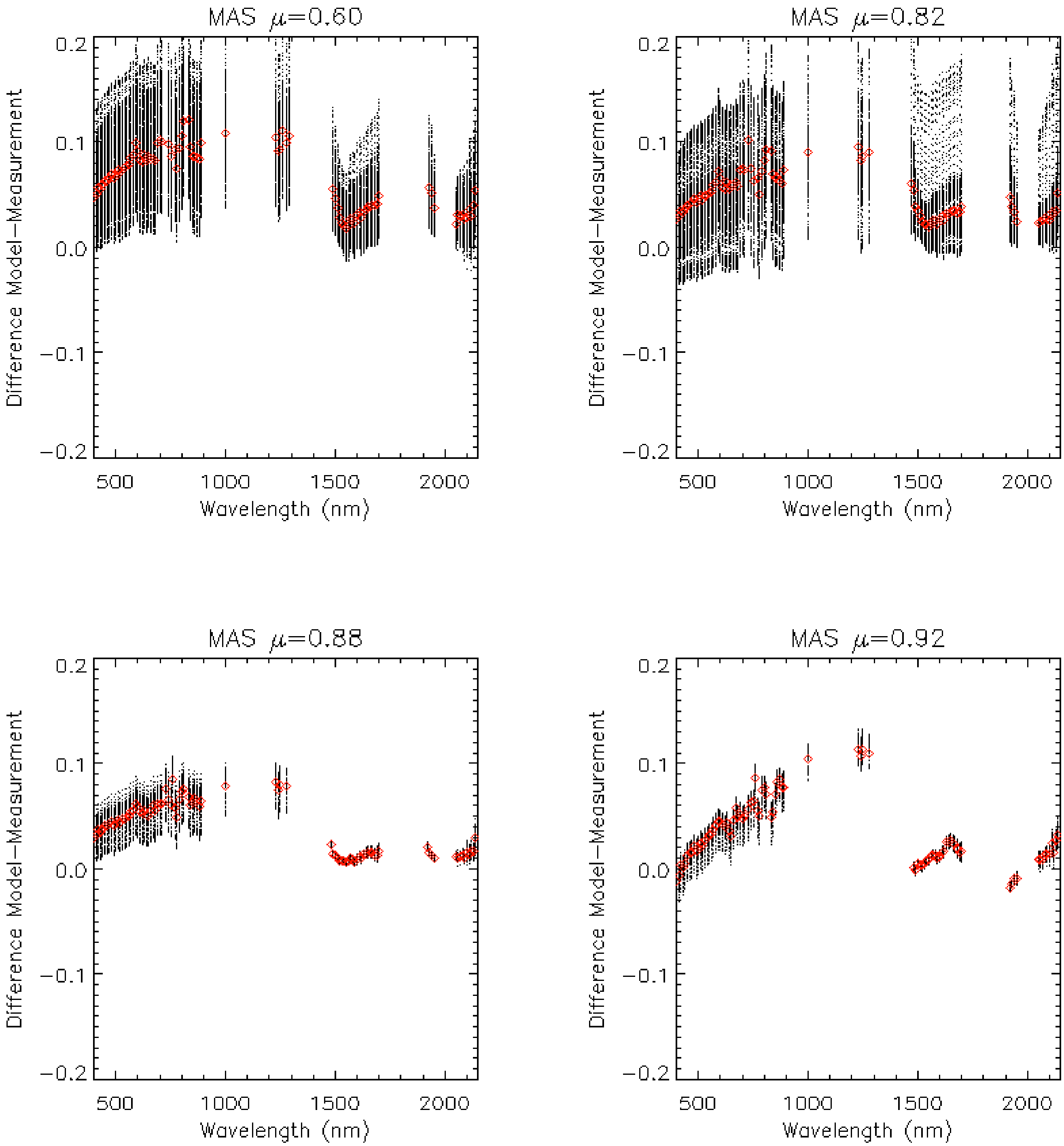

Figure 10. For each of the four cases, the difference between modeled and measured albedo, as parameterized by MAS is shown. The black dots are the differences for every line in the MAS flight track, the red diamond is the mean difference.

s.

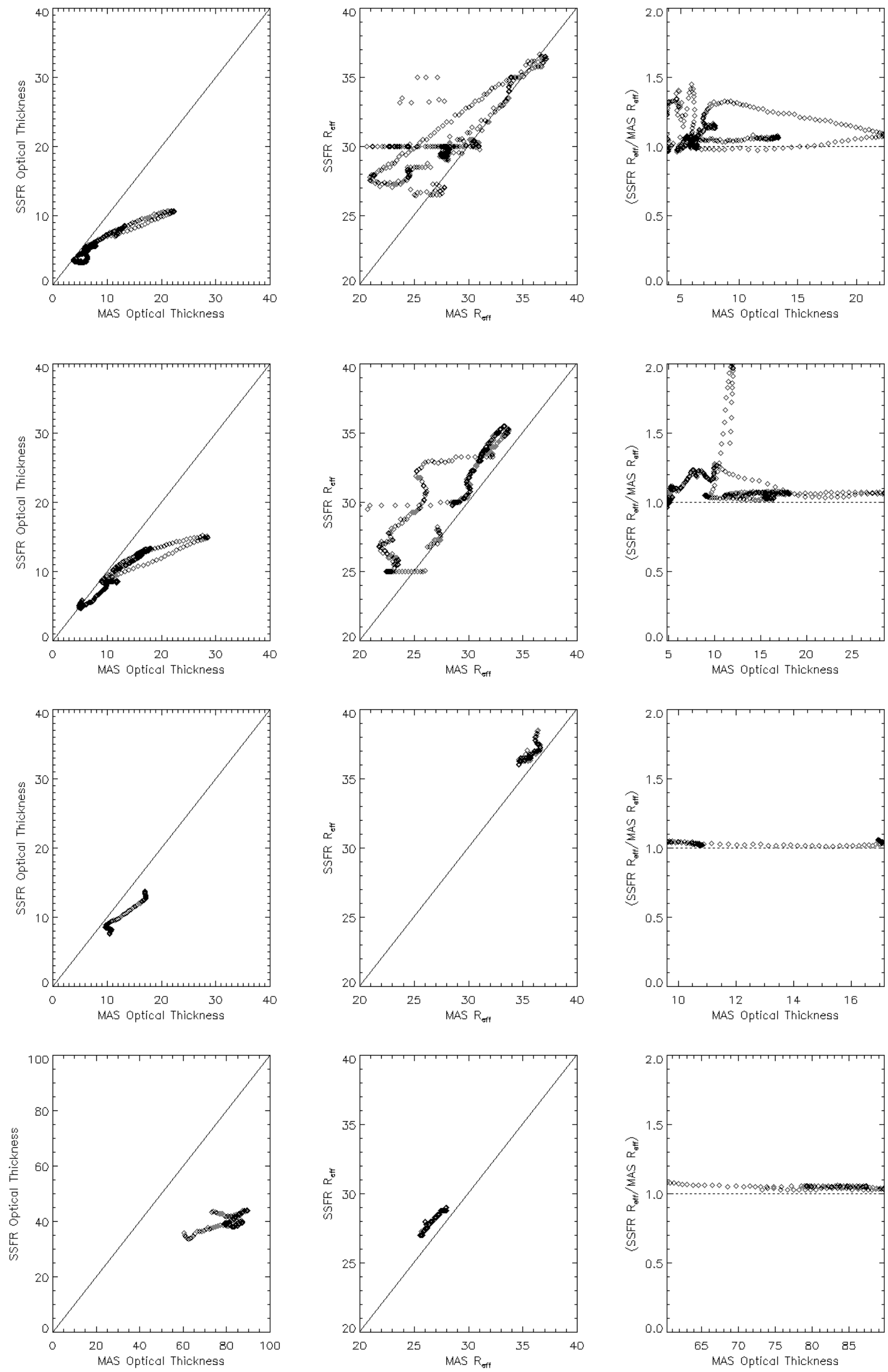

Figure 11. Optical thickness and effective radius as retrieved by SSFR and MAS are plotted against each other as is the ratio of effective radii from SSFR and MAS against optical thickness (third column). The top row is the μ=0.60, the second row μ=0.82, the third row μ=0.88 and the bottom row is μ=0.92. As optical thickness increases, the agreement between SSFR and MAS becomes better for effective radius.